The Heliconoides Modified Dissolution Index-HMDI: Do methane seepage environments affect the preservation state of Heliconoides inflatus?

Journal Article

Author(s):
Beccari, Valentina; Almogi-Labin, Ahuva; Basso, Daniela; Panieri, Giuliana; Makovsky, Yizhaq; Neururer, Christoph; Hajdas, Irka; Spezzaferri, Silvia

The *Heliconoides* Modified Dissolution Index-HMDI: Do methane seepage environments affect the preservation state of *Heliconoides inflatus*?

Valentina Beccari [a], Ahuva Almogi-Labin [b], Daniela Basso [c], Giuliana Panieri [d], Yizhaq Makovsky [e], Christoph Neururer [a], Irka Hajdas [f], Silvia Spezzaferri [a,*]

[a] *University of Fribourg, Department of Geosciences, Chemin Du Musée 6, 1700 Fribourg, Switzerland*
[b] *Geological Survey of Israel, Jerusalem 9692100, Israel*
[c] *University of Milano – Bicocca, Department of Earth and Environmental Sciences, CoNISMa, ULR of the University of Milano-Bicocca, Piazza della Scienza 4, 20126 Milano, Italy*
[d] *Department of Geosciences, CAGE–Centre for Arctic Gas Hydrate, Environment and Climate, UiT The Arctic University of Norway in Tromsø, Tromso, Norway*
[e] *Dr. Moses Strauss Department of Marine Geosciences and Hatter Department of Marine Technology, Leon H. Charney School of Marine Sciences (CSMS), University of Haifa, Haifa 3498838, Israel*
[f] *Laboratory of Ion Beam Physics, Swiss Federal Institute of Technology Zurich, CH-8093 Zurich, Switzerland*

ARTICLE INFO

ABSTRACT

Pteropods are holoplanktonic molluscs presently endangered because their fragile aragonitic shell is very sensitive to ocean acidification. The preservation of pteropods, and in particular of the mesopelagic *Heliconoides (Limacina) inflatus*, has been used to assess aragonite saturation state in Quaternary sediments (*Limacina Dissolution Index*, LDX) as an inferred proxy for climatic changes.

Three deep-sea cores retrieved in 2016 during the EUROFLEETS2 SEMSEEP cruise offshore Israel are investigated to assess the preservation degree of *H. inflatus* (d'Orbigny, 1835) in representative environments across the base of the southeastern Mediterranean margin (cold water coral, active seepage pockmark and deep sea channel areas). In some core intervals, yellowish, recrystallized internal molds of this species are present. They have been previously observed in the Eastern Mediterranean, but the nature and origin of their colour was never explained. Scanning Electron Microscopy (SEM), Energy Dispersive Spectroscopy (EDS) and Electron Backscatter Diffraction (EBSD) revealed that the recrystallized molds of the *H. inflatus* shells are formed by aragonite needles and high-Mg calcite crystals. The formation and preservation of these internal molds is induced by advective methane emissions, typically precipitating aragonite and High-Mg calcite phases close to the sediment–water interface. These molds were never used in previous applications of the LDX or in any existing ranking of pteropod preservation. Therefore, we have categorized these peculiar features combining previous pteropod ranking descriptions with the new observations to develop a modified biotic index (*Heliconoides* Modified Dissolution Index-HMDI).

High values of the HMDI at the base of the pockmark core correspond to the interval where also active seepage-related features – e.g., bubble emissions, low-oxygen benthic foraminifera, chemosymbiotic molluscs, small fragments of authigenic carbonate crusts and slightly depleted δ^{13}C values – occur, showing the applicability of the HMDI to methane seeps environments.

1. Introduction

Holoplanktonic molluscs are endangered organisms due to ocean acidification (OA). Their fragile aragonitic shell is very sensitive to this process due to the high solubility of aragonite (e.g., Bednaršek et al., 2012a; Bednaršek et al., 2012b). The cosmopolitan Euthecosomata pteropod *Heliconoides inflatus* (d'Orbigny, 1835) (previously named *Limacina inflata*) is a very common warm-water species. Its juveniles have an epipelagic stage, living in the top 100 m, whereas the adults become mesopelagic, reaching living depth below the thermocline at 350–250 m during the day, and migrating up to 50 m depth at night (Bè and Gilmer, 1977; Wormuth, 1981; Gerhardt and Henrich, 2001).

The preservation of pteropod shells has been widely studied to trace aragonite dissolution in late Quaternary sediments (e.g., Almogi-Labin et al., 1986; Gerhardt et al., 2000). Almogi-Labin et al. (1986) identified five categories, including internal molds and shells with secondary aragonite overgrowths. The *Limacina Dissolution Index* (LDX) was firstly developed by Gerhardt et al. (2000) based on the observations of Almogi-Labin et al. (1986). Their index is based on five categories, going from 'transparent shells' (stage 0) to 'opaque white, totally lustreless and perforated shells' (stage 5).

As Almogi-Labin et al. (1986) pointed out, the variability of pteropods preservation, the dissolution of their shells and the formation of internal molds in the sediments indicate the variation in carbonate chemistry of deep water and in bottom sediment interstitial waters. Thus, it derives from the combination of several factors, such as the amount of organic matter, anaerobic conditions and the consequent production of CO_2, denitrification and sulphate reduction in the sediments. These processes are common in methane-emission environments (e.g., cold seeps), where the waters are rich in methane and sulphates, resulting in the formation of high-Mg calcite carbonates (HMC); methane derived authigenic carbonates (MDAC), aragonite and euhedral gypsum crystals (Boetius et al., 2000; Panieri et al., 2017; Schneider et al., 2017, Schneider et al., 2018). Panieri et al. (2017) and Schneider et al. (2017), Schneider et al. (2018) document the presence of HMC inside benthic and planktonic foraminifera shells close to an active methane seep in the Vetsnesa Ridge (Western Svalbard) where the Sulfate-Methane Transition Zone (SMTZ) is close to the seafloor. Generally, HMC precipitates together with aragonite, during methane emission with high intensity flux (Aloisi et al., 2000; Greinert et al., 2001; Naehr et al., 2007; Schneider et al., 2018).

We investigate the morphology, chemistry and crystal orientation in different specimens of *H. inflatus* using different analytical techniques: visual classification, Scanning Electron Microscopy (SEM), Energy Dispersive Spectroscopy (EDS), Electron Backscatter Diffraction (EBSD).

The aim of this work is to understand the effect of seepage emissions and consequent changes in water chemistry on the preservation state of this species and to numerically express it with a modified index that results from the combination of the methods proposed by Gerhardt et al. (2000) and Almogi-Labin et al. (1986) and the addition of a new category.

2. Study area

The Levantine Basin (southeastern Mediterranean Sea) is ultra-oligotrophic. Its surface water mass (Levantine Surface Waters, LSW) has temperature and salinity seasonal variations ranging from ~15 °C to ~28 °C and 38.9 ‰ to 39.3 ‰, respectively (Hecht, 1992; Ozer, et al., 2017, Ozer et al., 2020). This is also reflected by the measurements of the 2016 SEMSEEPS cruise that is at the base of this study (Makovsky et al., 2016). Below the SLV the Modified Atlantic waters (MAW) have a thickness of 50–200 m and salinity of 38.6 ‰. The underlying Levantine Intermediate Water (LIW), formed in the Levantine Basin between 200 and 800 m depth have temperatures and salinities of 15 °C to 17 °C and ~39‰, respectively. Under the LIW lies the Eastern Mediterranean Deep-Water mass (EMDW), with relatively stable salinity of 38.7‰ and temperature of 13.35 °C (Fig. 1; Roether et al., 2007). The EMDW forms both in the Southern Adriatic cyclonic gyre (Skliris, 2014) and in the Aegean Sea (Hecht, 1992; Roether et al., 2007), with an abrupt recent switch occurring between them.

The Levantine Basin receives its primary supply of sediments and nutrients from the Nile River and is extremely sensitive to climatic changes (Almogi-Labin et al., 2009). Sediments and nutrients are directly transported to the basin floor through turbidite channels formed in the Nile Deep Sea Fan, and through an along-shore bypass along the southeastern Levant continental margin (Gvirtzman et al., 2015; Schattner and Lazar, 2016). The southeastern Levant seafloor is deformed due to the mobilization of sediments over the Messinian evaporites (Gvirtzman et al., 2015). In particular, Palmahim Disturbance (PD) is a large scale (20 × 10 km) salt rooted submarine rotational slide across the continental shelf and slope offshore southern Israel, between water depths of 70 and 1200 m (Garfunkel et al., 1979). On the northern margin of PD, between water depths of ~500 to 800 m, rocky authigenic carbonate outcrops, which are associated with paleo-
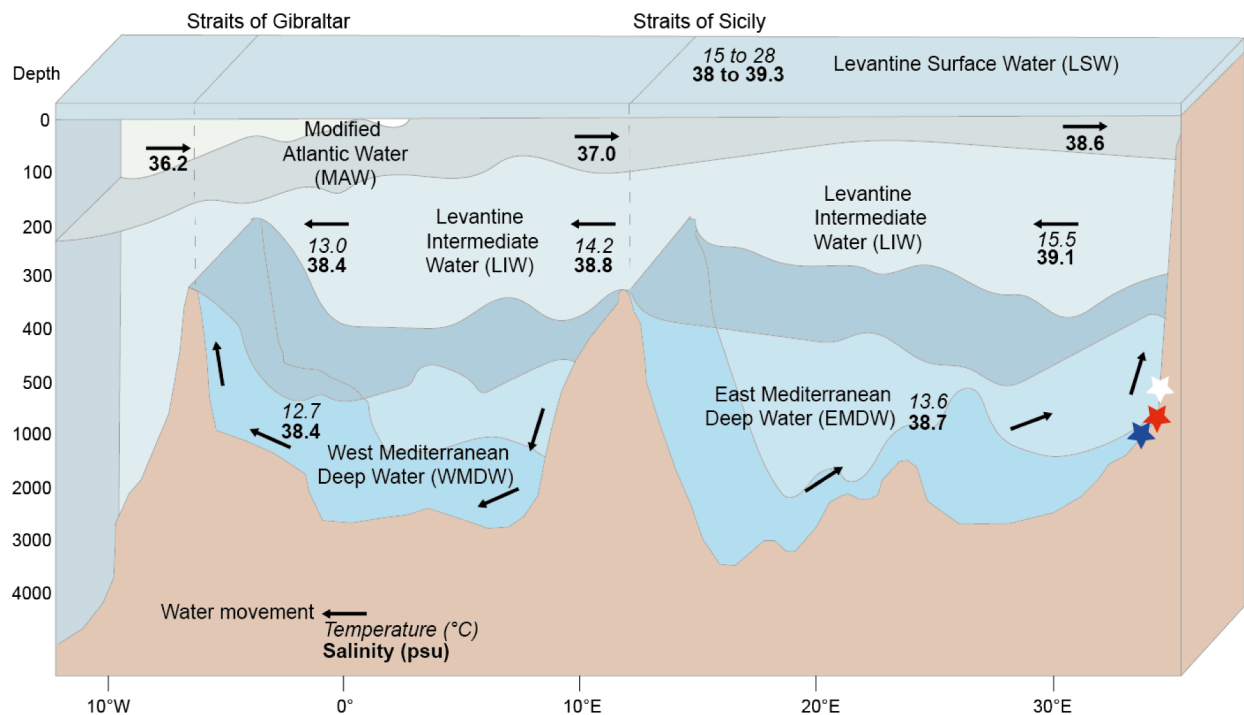

Fig. 1. Schematic summary of the vertical distribution of the Mediterranean water masses. Image modified after GRID-Arendal (https://www.grida.no/resources/5885) based on Zavatarelli and Mellor (1995). White star = Core AG16-20-BC1; Red star = Core AG16-23-BC2; Blue star = Core AG16-25-BC1a. (For interpretation of the references to color in this figure legend, the reader is referred to the web version of this article.)

seepage, served as settling grounds to multiple deep-sea corals and associated habitats (Coleman et al., 2012; Spiro et al., 2021). Several active seepage features, including carbonate crusts, bacterial mats, bivalve beds and chemosymbiotic living fauna, were documented within ~1 km scale pockmarks at the western toe region of PD (Coleman et al., 2012; Rubin-Blum et al., 2014; Basso et al., 2020; Beccari et al., 2020; Sisma-Ventura et al., 2022; Lawal et al., 2023).

3. Material and methods

Samples were collected during the EUROFLEETS2 SEMSEEP cruise (September 2016) onboard the R/V Aegaeo offshore Israel (Makovsky et al., 2016). A 30 × 30 cm box corer with a 60 cm penetration depth was used to obtain undisturbed samples. For this study, three cores from three representative areas were selected, the AG16-20-BC1b in the Coral area was collected at 690 m water depth. This Coral area will be hereafter called Coral-transition area because seep-related elements are also present in the core (e.g., ox-redox black and orange tubes, gypsum crystals). Core AG16-23-BC2 was collected in the Pockmark area at 1038 m water depth. Core AG16-25-BC1a was collected in a deep-sea channel of the Nile Deep Sea Fan, within Gal-C exploration block ~40 km west of PD, at 1310 m water depth (Fig. 2; Table 1). Sediments are dominantly composed by brownish pelagic clay, often intercalated with light and/or dark lenses. Surface sediments show slight (AG16-25-BC1a) to intense (AG16-23-BC) bioturbations (Makovsky et al., 2016).

Samples were investigated at two centimeters resolution. They were dried at open air, weighed, the volume was measured and then they were gently washed with a 32 μm mesh sieve. After washing and drying processes, residues were weighed. Grain size analyses (phi categories) were performed using dry sieving (500 μm, 250 μm, 125 μm, 63 μm and >32 μm). Pteropods and Heteropods were identified at species level and counted (Beccari et al., 2023). Following Gerhardt et al. (2000) a maximum of 40 specimens of *H. inflatus* were picked from the >250 μm fraction, samples with less than 10 specimens of *H. inflatus* were discarded. To assess the preservation state, light microscopy images of *H. inflatus* were taken on reference specimens with a Nikon SMZ18 microscope equipped with a camera and all other specimens were categorized accordingly.

Microstructural analysis of pteropod tests was carried out on selected specimens using Scanning Electron Microscopy (SEM, Thermo Fisher SEMFEIXL 30SFEG upgraded to remX Microscope control) at the University of Fribourg, after coating them with 40 nm of gold, using a high vacuum pump for at least 30′. Further Energy Dispersive X-ray Spectrometry (EDS, AZTec Advanced System with EDS Silicon Drift Detector XmaX 150 mm^2 with 127 eV energy resolution) and Electron Backscatter Diffraction (EBSD, HKL Advanced with a Nordlys camera and forescatter detector, with 4 diodes) micro-analyses were conducted to evidence the different chemical composition of the shells and crystal orientations. In particular, maps of the distribution of aragonite and calcite in the shells were obtained through EBSD analyses and elemental mapping with EDS.

Stable isotope analyses of benthic and planktonic foraminifera can provide important information about the chemical environment that affected shell formation and post-mortem diagenesis. Negative carbon isotopic peaks (δ^{13}C), may be due to local methane release (Torres et al., 2003) and the δ^{13}C signature of altered benthic foraminifera can be used to reconstruct the sulphate-methane transition zone (SMTZ) dynamics (e.g., Schneider et al., 2018; Panieri et al., 2016a; Panieri et al., 2016b).

The oxygen isotope composition (δ^{18}O) of planktonic and benthic assemblages reflects that of ambient seawater which depends mainly on temperature (McCrea, 1950), and on salinity (Craig and Gordon, 1965). Methane emissions may also affect δ^{18}O (Dessandier et al., 2020). The following species were used for isotope analyses: the planktonic foraminifera *Globigerinoides ruber* (d'Orbigny), and the benthic species *Uvigerina mediterranea* Hofker, *Uvigerina peregrina* Cushman, *Bulimina marginata* d'Orbigny, *Melonis barleeanum* (Williamson), *Chilostomella oolina* Schwager, and *Cibicides lobatulus* (Walker and Jacob). Samples were placed in 4.5 mL vials, flushed with He and H$_3$PO$_4$, equilibrated for more than two hours at 50 °C and then analysed on Gasbench II and MAT253 IRMS for δ^{13}C and δ^{18}O. Between 5 and 10 foraminiferal tests were picked from the 125–250 μm size fraction. Results were normalized to the Vienna PDB. The instrument uncertainty is standard deviation ≤0.1 permil (ThermoScientific).

Accumulation of organic matter can affect the preservation of the pterodopod shells and may give relevant information of surface productivity. A standard Rock-Eval 6 model (Vinci Technologies, Rueil Malmaison, France) was used to obtain the Total Organic Carbon (TOC %) and Carbonates wt. % at the University of Lausanne. Between 60 and 80 mg of sediments powder was used for each sample. The technique is
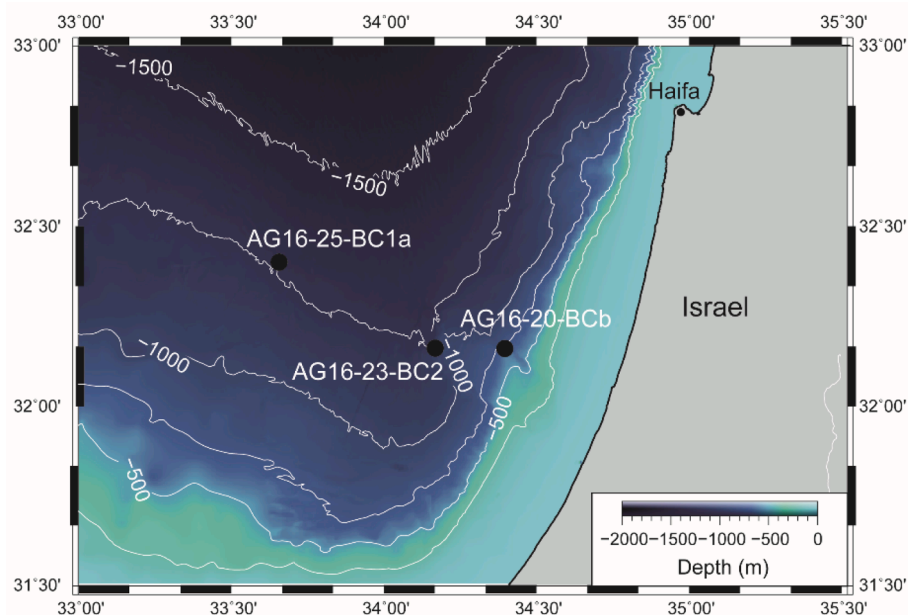

Fig. 2. Location map of the studied area (offshore Israel) showing the position of the cores AG16-20-BC1b (Coral-transition area), AG16-23-BC2 (Pockmark area) and AG16-25-BC1a (Gal-C deep-sea channel area). Map modified from Generic Mapping tools (GMT 5, Wessel et al., 2013).

Table 1
Geographical coordinates, studied interval, size fraction, and water depth of the core samples used in this study (from Makovsky et al., 2016).

Station	Location	Interval	Size fraction (μm)	Latitude (N)	Longitude (E)	Water depth (m)
AG16-20-BC1	N Palmahim Disturbance Coral site	Core 0–29 cm	>250	32°09.650′	34°23.700′	690
AG16-23-BC2	W Palmahim Disturbance Pockmarks	Core 0–38 cm	>250	32°09.650′	34°10.060′	1038
AG16-25-BC1a	Gal-C channel area	Core 0–37 cm	>250	32°24.010′	33°39.450′	1310

based on pyrolysis in an inert atmosphere followed by oxidation, using temperatures between 200 and 850 °C.

Radiocarbon dating was performed at the Eidgenössische Technische Hochschule (ETH) Zürich using the AMS accelerator mass spectrometer. The benthic foraminifera *Cibicides pachyderma* (Rzehak) was selected for core AG16-20-BC1b as it was the most abundant species; the planktonic foraminifera *G. ruber* and *Trilobatus sacculifer* (Brady) were selected for cores AG16-23-BC2 and AG16-25-BC1a, 1877). Specimens were picked from the fraction >250 μm, grouped to reach 4–12 mg of pure carbonate and cleaned in ultrasound bath for few seconds to remove any possible contamination. All results are corrected for $\delta^{13}C$ measured on graphite sample and expressed in radiocarbon age units i.e., BP = 1950 CE. Radiocarbon ages were calibrated using the Marine20 calibration curve (Heaton et al., 2020).

4. Results

4.1. Chemical analysis

Nine specimens of *H. inflatus* were tested for EDS and EBDS analyses. The results of four selected specimens best representing the different stage of preservations are documented in Figs. 3, 5-6.

4.2. Energy Dispersive X-ray (EDS) analysis

Microstructural and chemical analysis revealed three main shell preservation types: an original aragonitic shell still preserved (Fig. 3, n. 2), a recrystallized aragonite shell (Fig. 3, ns. 3,4) and an infilling sediment composed mainly by high-Mg calcite (Fig. 3, n.5). Several other elements, such as Sr, Si, Fe, Al, K, Ti, can be recognized only in smaller quantities in the indurated sediments infilling the shells (Supplementary Material 1).

4.3. Electron Backscatter Diffraction (EBSD) analysis

Chemical, microgranular and microstructural analyses supported the distinction of the aragonite and calcite phases of $CaCO_3$ (Fig. 3, ns. 2b-5b). Crystal orientation is presented on color maps, with the same color corresponding to the same orientation (Fig. 3, ns. 2e-5e). Thus, the EDS spectra analysis allowed to assess that: 1) both the original and the recrystallized shells were made by aragonite; 2) the aragonitic needles of the lithified and recrystallized shells follow a precise mirrored growth pattern going from the center of the lithified infilling towards the outer boundary of the shell (Fig. 3, ns. 3e-4e), whereas crystal orientation of the HMC phase shows a random growth pattern (Fig. 3, ns. 2e-5e).

When the original aragonitic shell was still preserved (Fig. 3, n. 2), the equipment was not able to detect the grains in the phase map (Fig. 3, n. 2b), probably due to the very fine size of the crystals. However, the aragonitic border is clearly shown in the Ca map (Fig. 3, n. 2c) as well as the infilling, where the amount of Mg is important (Fig. 3, n. 2d). The HMC infilling is more pronounced in specimen 5 (Fig. 3, n. 5) where the difference between aragonite and high-Mg calcite is very clear (Fig. 3, ns. 5b-5d). Some specimens with a recrystallized aragonite shell were also filled with aragonite needles and HMC crystals (Fig. 3, n. 3).

4.4. Scanning Electron Microscope (SEM) analyses

The Scanning Electron Microscope (SEM) analyses on selected specimens from the studied cores reveal differences in the wall structure of the shells in specimens with different preservation stages.

In particular, well-preserved specimens (Fig. 4a-b) show the original aragonitic helical structure of the shell. Minor dissolution features are recognized on the shell surfaces (Fig. 4a). In opaque lustrous and lusterless shells (Fig. 4 c-d) the aragonitic helical layer is not visible anymore and distinct dissolution features are recognizable on the shell surfaces. Internal molds are formed by aragonite needles filled with high-Mg calcite grains (Fig. 3, ns. 1–3, 4,5; Fig. 3g-h). Secondary aragonite overgrowths cover the internal molds of the shells (Fig. 3, n. 5; 3h).

4.5. Index values

4.5.1. The Heliconoides inflatus Modified Dissolution Index, HMDI

Pteropods were tentatively classified following Gerhardt et al. (2000) who refer exclusively to specimens with their original shell still preserved. These classes are: stage 0: transparent shells, stage 1: milky and cloudy shells, lustrous shell surface, stage 2: opaque-white shells, lustrous shell surface, stage 3: opaque-white shells, partly lustreless shell surface, stage 4: opaque-white shells, totally lustreless shell surface, stage 5: opaque-white shells, totally lustreless and perforated shell. The Gerhardt et al. (2000) classes are based on Almogi-Labin et al. (1986) categories: (i) transparent shells, (ii) opaque-white shells, (iii) internal molds with remnant original shell, (iv) internal molds, (v) secondary aragonite overgrowth. The protocol of Gerhardt et al. (2000) was tentatively applied to our samples. However, due to the presence of significant amounts of internal molds, it was soon clear that new categories were needed. Therefore, also the categories iii, iv and v described by Almogi-Labin et al. (1986) had to be considered.

We proceeded by steps initially identifying three different modes of shell preservation (Table 2):

- **Group (1)**: (Fig. 4) corresponds to stages 0-1-2 of Gerhardt et al. (2000) classification, going from well-preserved transparent to opaque and lustreless specimens. It corresponds to stages i and ii of Almogi-Labin et al. (1986).
- **Group 2**: (Fig. 4) this group includes some other characters described by Gerhardt et al. (2000) for stages 2–3; 4 and 5. All of them include specimens filled with lithified and recrystallized sediments, where high-Mg calcite is the dominant phase. The shells are not completely replaced but underwent various degrees of shell dissolution similarly to some of the features described for stage iii in Almogi-Labin et al. (1986) for specimens from the Red Sea.
- **Group 3**: (Fig. 4) includes pteropod shells changing into a yellowish colour coupled with intensive recrystallization that erase/remove the fine details of the original pteropod wall structure. These specimens were observed only in the bottom part of the pockmark core. In these specimens, the original aragonitic shell is replaced by fine-grained yellowish aragonite needles (stage iv-v of Almogi-Labin et al., 1986). This group did not match any group in Gerhardt et al. (2000) classification.

Based on these characters and the poor correspondence with previously described preservation stages of Gerhardt et al. (2000), and Almogi-Labin et al. (1986) seven more detailed stages of pteropods preservation (Fig. 4) were identified and integrated in a modified index composed by preservation stages 0 to 7: the *H. inflatus* Modified
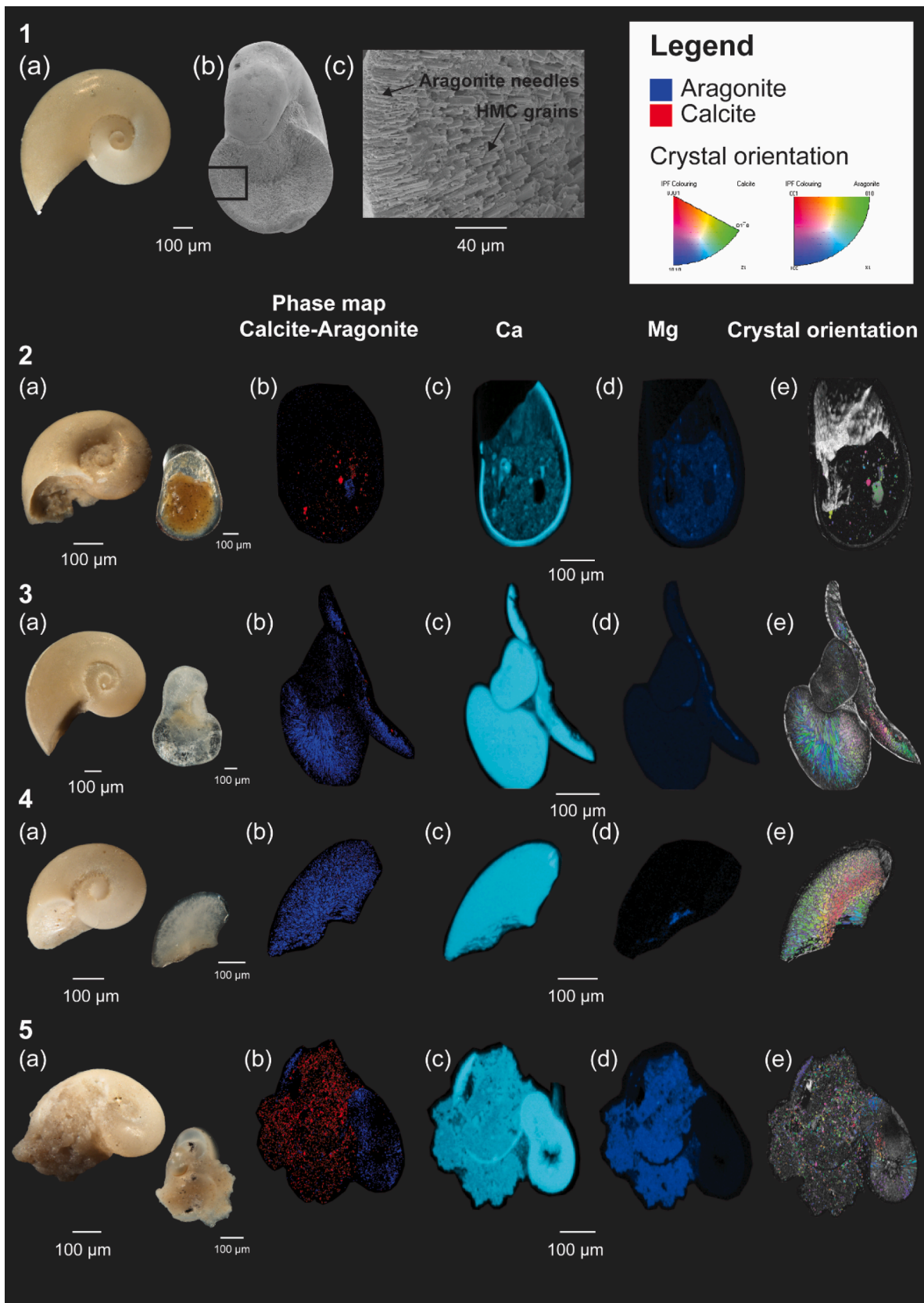
Fig. 3. Illustration of 5 selected specimens used for EDS and EBDS analysis. 1. (a) Light microscope and (b) SEM images of recrystallized *H. inflatus,* (c) close up on aragonite needles and HMC crystals. 2–5 (a) Light microscope images of the specimens and miniature of the polished specimen used for the analyses, (b) phase maps of aragonite (blue) and calcite (red), (c) Ca elemental maps, (d) Mg elemental maps and (e) crystal orientation maps. Note that same color corresponds to same crystal orientation. (For interpretation of the references to color in this figure legend, the reader is referred to the web version of this article.)
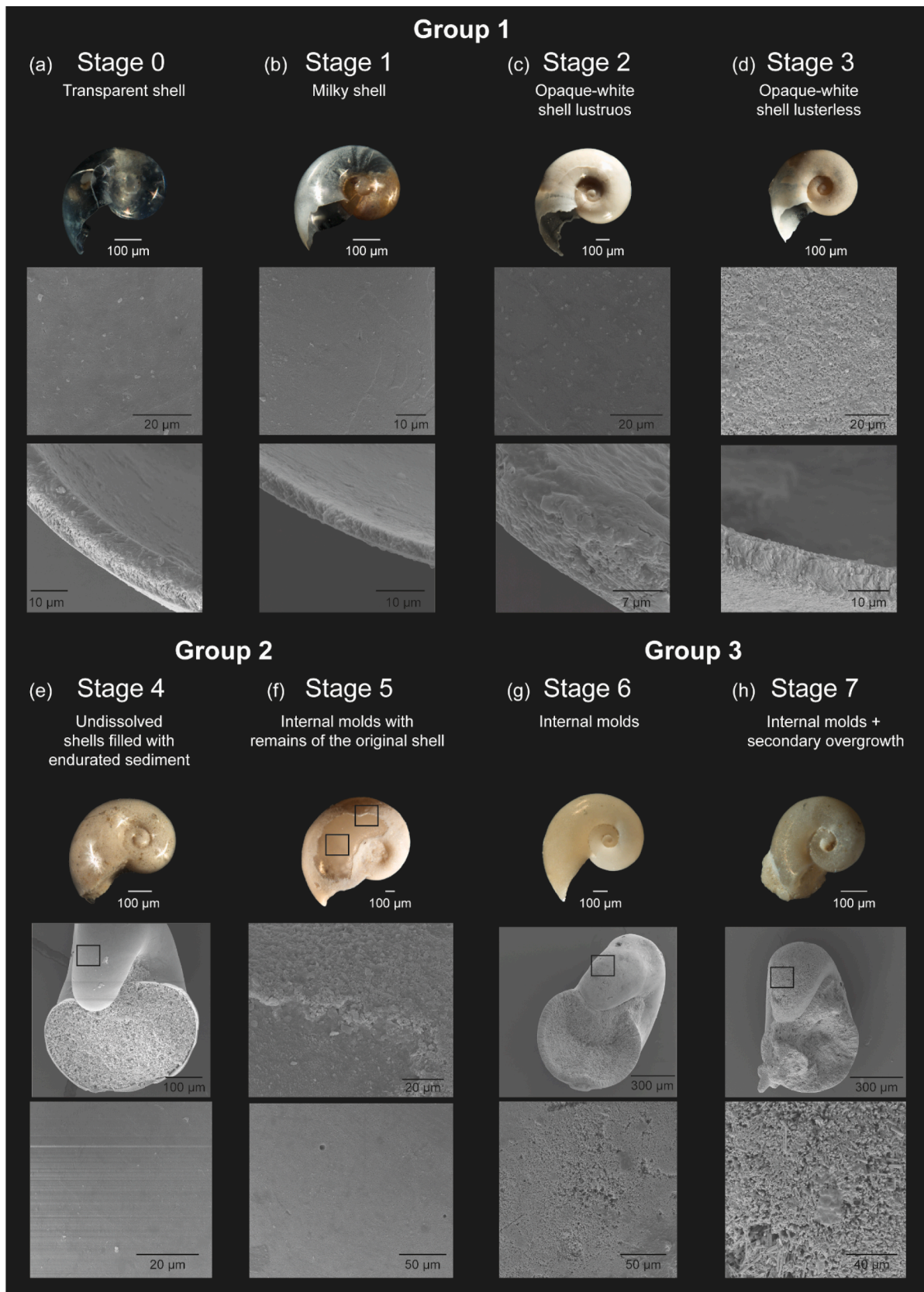
Fig. 4. Seven stages of the *H. inflatus* Modified Dissolution Index (HMDI). Group (1) includes (a) stage 0, transparent shell; (b) stage 1, milky shell; (c) stage 2, opaque-white shell lustrous; (d) stage 3, opaque-white shell lusterless. Group 2 includes (e) stage 4, undissolved shells filled with endurated sediment. Group 3 includes (f) internal molds with remains of the original shell; (g) internal molds; (h) Internal molds covered by secondary overgrowth.
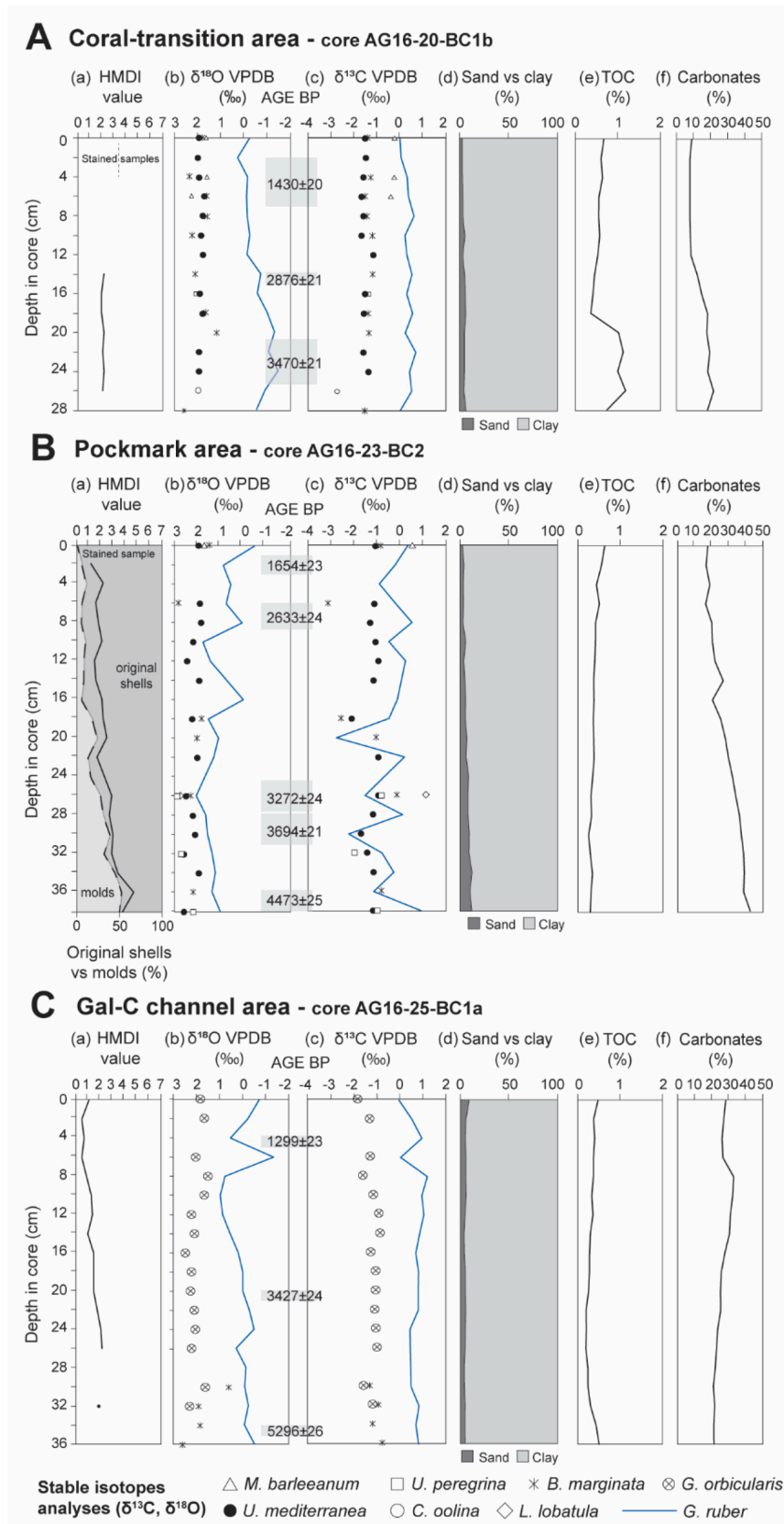
Fig. 5. HMDI, stable isotopes, grain size, TOC and % carbonates in the investigated cores. (a) *H. inflatus* Modified Index values in the cores; (b-c) stable isotopes (δ^{18}O and δ^{13}C) measured on benthic and planktonic foraminifera and AMS^{14}C dating; (d) percentages of sand vs clay; (e) Total Organic Carbon (TOC wt. %); (f) Carbonates wt %.
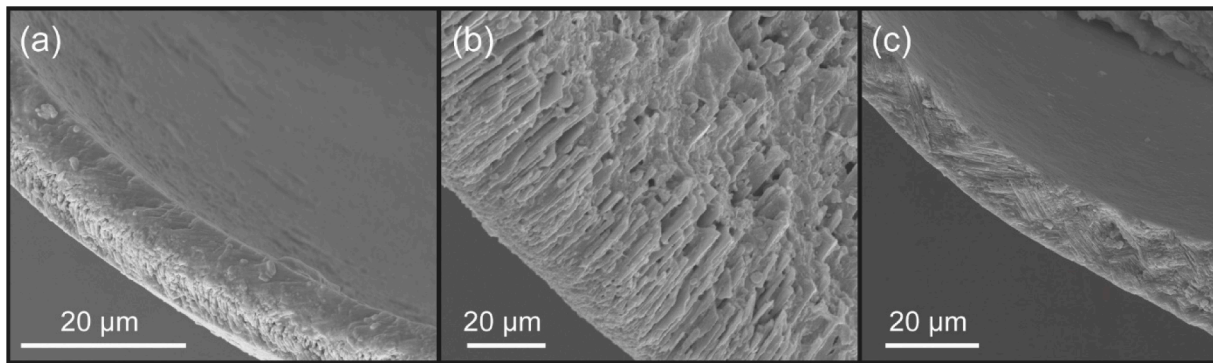
Fig. 6. Comparison of the wall structure. (a) *H. inflatus* helical layer; (b) *H. inflatus* recrystallized aragonite (c) *Limacina bulimoides* crossed lamellar layer.

Table 2
Summary of the groups and categories of pteropod preservation used by Almogi-Labin et al. (1986), Gerhardt et al. (2000) and in the present study (Figs. 3 and 4).

Groups	Almogi-Labin et al. (1986)	Gerhardt et al. (2000)	Present study
Group (1)	i. Transparent shells	0.Transparent shells	0. Transparent shell
	ii. Opaque-white shells	1. Milky and cloudy shells, lustrous shell surface	1. Milky shell
		2. Opaque-white shells, lustrous shell surface	2. Opaque shell lustrous
Group 2	iii. Internal molds with remnants of original shell (pro parte)	3. Opaque-white shells, partly lustreless shell Surface	3. Opaque shell lustreless
		4. Opaque-white shells, totally lustreless shell Surface	4. Undissolved shell filled with indurated sediments
		5. Opaque-white, totally lustreless and perforated shells	5. Internal molds with remnants of the original shell still preserved (pro parte)
Group 3	iv. Internal molds v. Secondary aragonite overgrowth:		6. Internal molds 7. Internal molds with secondary overgrowth

Dissolution Index - HMDI.

- Stage 0: Transparent shell
- Stage 1: Milky shell
- Stage 2: Opaque shell lustrous
- Stage 3: Opaque shell lustreless
- Stage 4: Undissolved shell filled with indurated sediments
- Stage 5: Internal mold with remnants of the original shell still preserved
- Stage 6: Internal mold
- Stage 7: Internal mold with secondary overgrowth

From the original equation of Gerhardt et al. (2000):

$$LDX = S(n_p p)/Sn_p \qquad (1)$$

with p = 0–5, where n_p is the number of investigated tests per preservation stage and p is the value of the preservation stage (p = 0–5).
Maintaining the same coefficients, the HMDI modified equation becomes:

$$\mathrm{HMDI} = \Sigma(n_p p)/ \Sigma n_p \qquad (2)$$

with p = 0–7, the number of stages (p), increase to p = 0–7

(Supplementary Material 2).

4.5.2. Coral-transition area (core AG16-20-BC1b)

The HMDI could be calculated only for seven samples (from 14 to 27 cm), where it presents the minimum statistically valid abundance of *H. inflatus*. The original aragonitic shells with an opaque-white lustrous shell are preserved in all specimens. The HMDI value range from 2 to 2.2 (Fig. 5A). The highest sand-fraction content value (5%, Fig. 5A) is observed at the base of the core (28–29 cm). δ^{13}C values measured on selected benthic foraminifera vary from 0.59‰ to −2.47‰ (Fig. 5A), while the planktonic foraminifera values range from 0.04 to 0.74‰ (Fig. 4A; Supplementary Material 3). The δ^{18}O of benthic foraminifera ranges from 1.15 to 2.57‰ while those of planktonic foraminifera varies from −0.09 to −1.43‰ (Fig. 5A; Supplementary Material 3). The TOC wt. % values are relatively constant from 0 to 19 cm, ranging from 0.34 to 0.64%. The highest TOC wt. % values are registered from 19 cm to the base of the core, ranging from 0.72 to 1.16 (Fig. 5A). Carbonate wt. % also follows the same trend, ranging from 7.82% on top and increasing downcore, up to 21.8% (Fig. 5A).

The AMS ^{14}C dating indicate an age of 1430 ± 20 BP between 2 and 7 cm, 2875 ± 21 BP at 15 cm and 3470 ± 21 BP between 22 and 25 cm (Fig. 5A, Table 3).

4.5.3. Pockmark area (core AG16-23-BC2)

The HMDI could be assessed for all samples. The values range from 1.2 to 4.7 (Fig. 5B). The lowest portion of the core contains the highest abundances of recrystallized aragonite specimens, filled with high-Mg calcite sediments (Fig. 3, n. 1, Fig. 5B). In the Pockmark core the highest sand fraction content (13%, Fig. 5B) is at 34–35 cm. In the lowest part of the core a large number of small fragments of authigenic carbonate crusts bivalve shells and shrimp claws (*Calliax* sp.) occur, decreasing upcore and disappearing at the top. The heaviest δ^{13}C values (around 1‰) of benthic foraminifera are measured in the central part and at the base of the core, in correspondence with some of the lowest HMDI values (Fig. 5B). Values range from positive (1.13‰) to negative in the lower part of the core (-3.11‰; Fig. 5B). Carbon isotope data for *G. ruber* ranged from −2.11 to 0.98‰ (Fig. 5b, blue line). The δ^{18}O values of benthic foraminifera are positive, varying between 1.43 and 2.91‰ (Fig. 4B). Oxygen isotopes for *G. ruber* are all positive (0.09 to 2.04‰; Fig. 4B, blue line), with the only exception of the surface sample (-0.44‰; Fig. 5B, Supplementary Material 3).

The TOC wt. % values are constant throughout the core (0.24–0.62%; Fig. 5B). Carbonate wt. % values are higher in the lower part of the core (17.10–42.97 %, Fig. 5B, Supplementary Material 3).

The AMS ^{14}C dating based on mixed planktonic foraminifera *G. ruber* and *T. sacculifer* provide an age between 1654 ± 23 BP and 4473 ± 25 BP at 37 cm (Fig. 5B; Table 3).

4.5.4. Gal-C channel area (core AG16-25-BC1a)

A pteropod ooze characterizes the top of this core, being dominated

Table 3
Radiocarbon AMS ^{14}C dating on benthic (Bf, *C. pachyderma*) and planktonic (Pf, *G. ruber* and *T. sacculifer*) foraminifera obtained from cores AG16-20-BC1b, AG16-23-BC2 and AG16-25-BC1a.

Core	Core depth (cm)	Material	Sample ID	^{14}C-age (BP)	± 1σ	δ^{13}C value (AMS) (VPDB ‰)	Calibrated Interval (cal BP)
AG16-20-BC1b	2–7	Bf-*Cibicidoides pachyderma*	ETH-115056	1430	20	1.1	1171–740
AG16-20-BC1b	14–15	Bf-*Cibicidoides pachyderma*	ETH-115057	2876	20	1.0	2850–2369
AG16-20-BC1b	22–25	Bf-*Cibicidoides pachyderma*	ETH-115058	3470	21	2.6	3581–3101
AG16-23-BC2	0–5	Pf-*G.ruber* and *T.sacculifer*	ETH-117606	1654	23	2.3	1380–969
AG16-23-BC2	6–9	Pf-*G.ruber* and *T.sacculifer*	ETH-117607	2633	24	0.5	2610–2076
AG16-23-BC2	26–27	Pf-*G.ruber* and *T.sacculifer*	ETH-117608	3272	24	1.0	3354–2850
AG16-23-BC2	28–29	Pf-*G.ruber* and *T.sacculifer*	ETH-117609	3694	24	2.0	3867–3372
AG16-23-BC2	36–37	Pf-*G.ruber* and *T.sacculifer*	ETH-117610	4473	25	1.0	4880–4372
AG16-25-BC1a	4–5	Pf-*G.ruber* and *T.sacculifer*	ETH-117611	1299	23	2.4	1035–635
AG16-25-BC1a	20–21	Pf-*G.ruber* and *T.sacculifer*	ETH-117612	3427	24	3.2	3537–3048
AG16-25-BC1a	34–35	Pf-*G.ruber* and *T.sacculifer*	ETH-117613	5296	26	1.7	5865–5396

ΔR = -152 ± 79 was used for marine reservoir correction in calibrated ages.

by very well preserved and transparent pteropod shells. However, the HMDI could not be calculated for all core intervals due to low abundances of *H. inflatus* in some of the samples. Its values increase downcore, ranging from 0.5 at the top to 2.2 at the base (Fig. 5C). The maximum sand content is recorded at the top of the core, reaching about 8% of the total sediment. At the bottom of the core pyritized orange and black tubes are present, together with pyritized benthic and planktonic foraminifera. The δ ^{13}C values are negative and range from −0.77 to −1.83 ‰ for benthic foraminifera (Fig. 4c, Supplementary Material 2) and from −0.034 to 1.07‰ for *G. ruber* (Fig. 5C, solid blue line). The δ^{18}O of benthic foraminifera range from 0.57 to 2.48‰ (Fig. 5C, Supplementary Material 3) and from −1.36 to 0.98‰ for *G. ruber* (Fig. 5C, solid blue line). The TOC wt. % values are constant throughout the core (0.20–0.51%; Fig. 5C). Carbonate wt. % shows a slight increase from 8 to 17 cm (27.98–33.23%; Fig. 5C).

The AMS ^{14}C dating on *G. ruber* and *T. sacculifer* provide an age of 1299 ± 23 BP at 5 cm; 3427 ± 24 BP at 21 cm; and 5296 ± 26 BP at 35 cm (Fig. 5C, Table 3).

5. Discussion

5.1. Radiocarbon age

The differences in radiocarbon ages between surface dwellers planktonic foraminifera and benthic foraminifera can be used to trace paleo-circulation patterns in the deep-sea (e.g., Broecker et al. 1988; Ohkushi et al., 2017; Missiaen et al., 2020). However, sedimentation and paleo/oceanographic processes, and mixing effects may prevent a good interpretation of ocean ventilation reconstructions in low sedimentation settings (Missiaen et al., 2020). The three cores from the Palmahim Disturbance were dated using benthic foraminifera for Core AG16-20-BC1b and planktonic foraminifera for the other two cores because the residues did not contain sufficient benthic specimens, therefore, a bias in age determination may be expected. However, the ages of the top layers of Core AG16-20-BC1b (2–7 cm) dated with benthic foraminifera and AG16-23-BC2 (0–5 cm) dated with planktonic foraminifera are very close with only a difference of ca. 200 ^{14}C yrs (Table 3). Additionally, the age of the benthic foraminifera is younger, and this point toward a certain variability in the reservoir age in the mixed layer. This variability can be explained with the vertical sinking and lateral transport of particulate carbon occurring also today in the Levantine Basin and reaching water depth exceeding 1500 m (Alkalay et al., 2000). Also, the location of the sampling sites close to the coasts may have played a role in the carbon reservoir mixing and for such close reservoir ages between benthic and planktonic foraminifera.

5.2. Pteropod dissolution

Pteropods are good indicators of carbonate dissolution caused by

ocean acidification during their life in the water column (Bednaršek et al., 2012a, Bednaršek et al., 2012b). They are indicators of water corrosiveness when their aragonitic shells start to dissolve while sinking through the water column (Byrne et al., 1984), getting deposited at the sediments water interface (Adelseck and Berger, 1975) and being buried in the sediments (Almogi-Labin et al., 1986; Gerhardt et al., 2000; Gerhardt and Henrich, 2001; Manno et al., 2007).

Oakes et al. (2019) demonstrated that shell dissolution is controlled by the degradation of the organic matter composing the soft body of pteropods, turning the shell from glassy to slightly milky about 3.5 days after the death of the organisms. However, long-term dissolution depends on many factors, such as the undersaturation of water, corrosiveness of the water, shell size, sinking speed, local sedimentation rate, bottom current velocity and bacterial activity, microbial degradation of the organic matter in the sediments (Archer and Maier-Reimer, 1994; Martin and Sayles, 1996; Gerhardt et al., 2000).

Gerhardt et al. (2000) describes several cases of LDX inapplicability due to the absence of *Heliconodes* tests below 3400 m, which is the average North Atlantic Aragonite Compensation Depth (ACD), and at shallower depths along continental margins, where higher amount of organic matter facilitates the dissolution of the aragonite (Berger, 1978).

In the northern Red Sea the water column is super-saturated (Ω > 2.5, at 1100 m depth; Krumgalz and Erez, 1984; Almogi-Labin et al., 1986) and dissolution does not occur in deep waters. Thus, the poor preservation of pteropods can be explained by different rates of organic matter oxidation (Berger, 1979; Almogi-Labin et al., 1986, Gerhardt et al., 2000).

Almogi-Labin et al. (1986) and Gerhardt et al. (2000) mentioned that Limacinidae (Heliconoididae) show species specific dissolution susceptibility. *Heliconoides inflatus* possesses the thickest shell, composed by a central helical layer, and it is the most soluble and fragile compared to the thinner shell of *Limacina trochiformis* (d'Orbigny) or *Limacina bulimoides* (d'Orbigny) with a central layer composed of crossed-lamellar aragonite (Van Der Spoel, 1972, 1976; Richter, 1976; Bè and Gilmer, 1977; Bandel et al., 1984; Fig. 6). Preservation may also depend on very low supply of organic matter to the sediments and consequently limited CO_2 production, or high supply of organic matter and reduced ventilation (e.g., Gerhardt et al., 2000).

The Mediterranean and the Red Sea are defined as "carbonate traps" (Berger, 1978). In the Eastern Mediterranean the ACD is reported to be at about 3000 m deep (Berger, 1978; Rutten, 2001). The sediments investigated here from the Palmahim Disturbance were retrieved at a much shallower water depth, ranging from 690 to 1310 m), therefore the ACD cannot account for pteropod dissolution.

In the investigated samples various degrees of dissolution are found (Figs. 3-4, 6; Table 2). The best preservation also supported by positive values of HMDI between 2 and 3, is observed in In the Gal-C channel area where pteropods experienced normal dissolution processes with high abundance of transparent, milky and opaque lustrous shells

(preservation stages 0–3, Supplementary Material 2). The HMDI values are constant and vary from 2 to 3 (Fig. 5C, Table 2). No significant correlation with TOC, sand/clay, carbonate or stable isotope is observed in the Gal-C channel area (Fig. 5Cb, 5Ce, 5Cf). The $\delta^{18}O$ signature of *G. ruber* values (Fig. 5B) is similar to the signal measured in interglacial intervals in the Eastern Mediterranean, which usually oscillates between −1 and 1‰ (e.g., Hennekam, 2015; Mojtahid et al., 2015).

In the Coral-transition area rare transparent, milky and opaque lustrous coexist with lustreless shells (preservation stages 0–3) and recrystallized shells are absent (Supplementary Material 2). Nevertheless, the HMDI could be calculated only for one interval (Fig. 6B, Table 2) because shells of *H. inflatus* >250 μm were missing in most samples from 14 to 26 cm in the core. This interval corresponds also to higher TOC and carbonate values (Fig. 5Ae, 5Af), exceeding 1% and 15%, respectively. Beccari et al. (2023) interpreted this enrichment of organic matter as the consequence of coastal upwelling, resulting with enhanced biomass at the surface and organic matter accumulation at the sea floor. The more negative values of the $\delta^{18}O$ (Fig. 5Ab) support the hypothesis of cooler waters upwelled at the surface.

A different scenario can be inferred for the Pockmark area, where active methane seepage occurs. Yellow internal mold of pteropods are present from the base to the top of the core with increased abundance from 24 to 36 cm in the sediments corresponding to the AMS^{14}C interval 4443–3272 yrs, while the other preservation categories vary in abundance (Supplementary Material 2).

Internal molds of planktonic organisms are frequent in sediments of enclosed basins, such as the Mediterranean and the Red Sea (Friedman, 1965; Milliman et al., 1969) and are generally composed of irregular rhombus of HMC. These can be detrital, or in most cases authigenic (Milliman et al., 1969). Their formation requires special microenvironments inside the shell (Almogi-Labin et al., 1986, 2008). The extreme dissolution may lead to the complete disappearance of the aragonitic pteropod shell, with consequent preservation of internal molds (Fig. 3). In the Red Sea, Almogi-Labin et al. (1986) measured a content of MgCO$_3$ up to 10–15% in HMC lithic fragments contained in molds, and similar HMC compositions were found by Milliman et al. (1969). They suggested a close relationship between aragonite dissolution and HMC precipitation, which may possibly be rapid and contemporaneous with shells filling. Schneider et al. (2017) describe benthic foraminifera that experienced dissolution and recrystallization with opaque yellowish shells from a site close to active methane seeps in the Western Svalbard with a SMTZ close to the sea floor. Notably, the co-occurrence of yellowish internal molds with authigenic carbonates was also reported by Hovland et al. (2005) in deep water off mid-Norway. The yellowish color of the internal mold of pteropods occurring in the Pockmark area (Figs. 3-4), is similar to that described by Schneider et al. (2017). In the Pockmark area the $\delta^{18}O$ values are more positive with respect to the Coral-transition and Gal-C channel area. Moreover, the $\delta^{13}C$ curve shows more negative peaks up to −3 ‰ with respect to the Coral-transition and Gal-C channel area. In agreement with (Torres et al., 2003) these negative carbon isotopic peaks are interpreted as related to local methane release. Recently the investigation of Dessandier et al. (2020) have demonstrated that also anomalous $\delta^{18}O$ values can possibly relate to methane emissions, therefore suggesting that the anomalously more positive $\delta^{18}O$ values identified in the Pockmark region are associated with methane seepage. We, therefore, suggest that the yellowish molds found in the pockmark area core are associated with methane seepage.

5.3. Nature of seep flux in the Palmahim Disturbance

In methane-seepage environments, microfossils can act as nucleation points for precipitation of methane derived authigenic carbonates (Panieri et al., 2016a; Panieri et al., 2016b; Schneider et al., 2017), e.g., aragonite (Kastner et al., 1990; Ambrose et al., 2015; Schneider et al., 2018) and high-Mg calcite (Burton, 1993; Schneider et al., 2018). These

carbonate phases precipitate within the sediments in the vicinity of a SMTZ (Aloisi et al., 2000; Ambrose et al., 2015; Schneider et al., 2018; Borrelli et al., 2020). Aragonite is often the dominant component such as found in the PD molds, in authigenic carbonates that forms where vigorous methane fluxes occur (Peckmann et al., 2001; Luff et al., 2004; Ambrose et al., 2015; Fig. 7).

Another evidence of seep influence on pteropods preservation in the Pockmark area is the co-occurrence of their molds with other seep-related features (Basso et al., 2020) including small fragments of authigenic carbonate crusts, opaque and dark colored planktonic foraminiferal shells, orange, red and black tubes and chemosymbiotic macrofauna. The latter include e.g., *Isorropodon perplexum* Sturany, 1896, *Waisiuconcha corsellii* Basso, Beccari and Spezzaferri, *Idas* sp. and *Taranis moerchi* (Malm, 1861) and the low oxygen tolerant benthic foraminifera *Globobulimina pseudospinescens* (Emiliani, 1949) and *Chilostomella oolina* Schwager, 1878 (Basso et al., 2020). This co-occurrence also testifies for variability in the methane flux intensity in this area, varying from advective, with high-intensity flux, precipitating aragonite minerals, to diffusive, supporting the settlement of the chemosymbiotic benthic faunal assemblage (Fig. 7).

In the Pockmark area, the aragonite composition of pteropod molds suggests that their formation may have been induced by advective methane emissions (Fig. 7), typically precipitating aragonite and High-Mg calcite phases close to the sediment water interface. The lowest HMDI coincides with abundant seepage features (Fig. 5B) evidencing the link with the methane-emission. It therefore, validates the applicability of the HMDI not only in normal marine environments but also in cold seeps. The important advantage of using the HMDI is that it considers internal molds, which are a significant component in these unique environments.

6. Conclusions

The preservation state of pteropods shells is important as a proxy to understand bottom water chemistry in the sediments after their sinking to the seafloor. The previously established LDX is a reliable indicator of aragonite dissolution in pristine environments, not subject to high productivity, degradation of organic matter and increase of bottom water CO$_2$. In this work, we demonstrate that with a minor implementation, the index can be useful also in other environments, subject to major modifying processes (e.g., methane emission), which are able to form and preserve internal molds of *H. inflatus*. We propose here a new biotic index: the *Heliconoides* Modified Dissolution Index-HMDI.

The internal molds of *H. inflatus* observed in this study, are composed mainly by aragonite needles and High-Mg calcite grains, phases typically formed during an advective methane emission. Therefore, low values of the HMDI, expressing their presence, could be a reliable tool to identify past methane emissions that supplement other sedimentary. The HMDI was successfully tested on the Palmahim Disturbance sediments, where other seepage-relates features corroborate the interpretation of methane emission. Therefore, we suggest that the HMDI can be used to assess dissolution related to the aragonite saturation, and to trace advective methane emissions.

CRediT authorship contribution statement

Valentina Beccari: Conceptualization, Methodology, Validation, Formal analysis, Investigation, Writing – original draft. **Ahuva Almogi-Labin:** Conceptualization, Methodology, Validation, Writing – review & editing. **Daniela Basso:** Conceptualization, Methodology, Writing – original draft, Writing – review & editing. **Giuliana Panieri:** Conceptualization, Validation, Writing – review & editing. **Yizhaq Makovsky:** Resources, Writing – review & editing. **Christoph Neururer:** Investigation, Writing – review & editing. **Irka Hajdas:** Investigation, Writing – review & editing. **Silvia Spezzaferri:** Conceptualization, Methodology, Validation, Writing – original draft, Writing – review & editing.
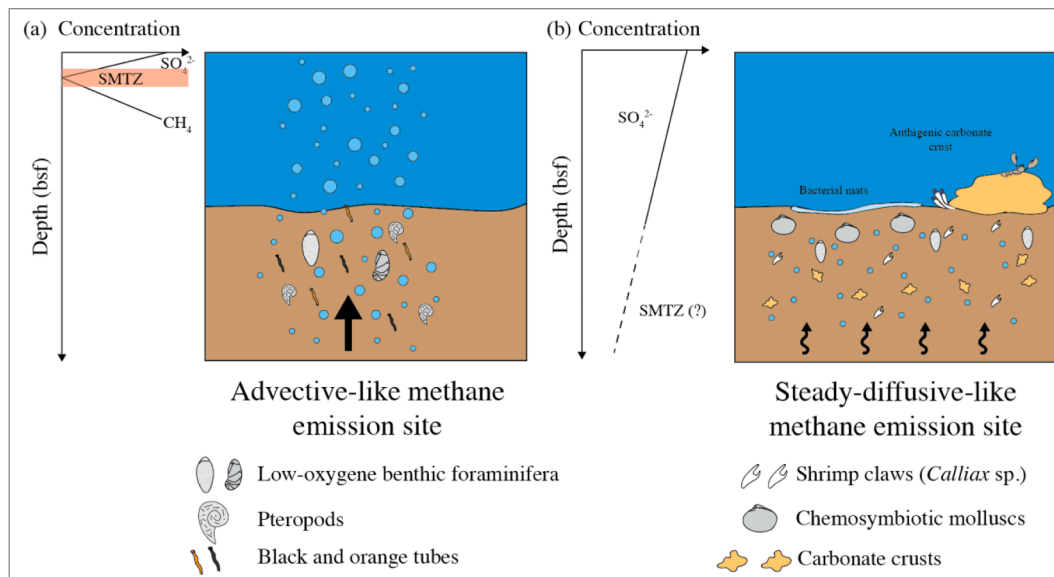
Fig. 7. Schematic representation of seepage site with an (a) advective emission, and (b) diffusive emission, plotted against the position of the SMTZ close to the seafloor and deep in the sediments, respectively.

Declaration of Competing Interest

The authors declare that they have no known competing financial interests or personal relationships that could have appeared to influence the work reported in this paper.

Data availability

All data are included as Supplementary Material

Appendix A. Supplementary data

Supplementary data to this article can be found online at https://doi.org/10.1016/j.ecolind.2023.110380.

References

Adelseck, C.G., Berger, W.H., 1975. On the dissolution of planktonic foraminifera and associated microfossils during settling and on the sea floor. In: Sliter, W.V., BØ, A.W. H., Berger, W.H. (Eds.), Dissolution of deep-sea carbonates, 13. Cushman Found Foraminiferal Research Special Publication, Ithaca, New York, pp. 70–81.

Alkalay, R., Zlatkin, O., Katz, T., Herut, B., Halicz, L., 2000. Berman-Frank, I. and Weinstein, Y.: Carbon export and drivers in the southeastern Levantine Basin. Deep Sea Res., Part II: Topical Studies in Oceanography, 171, 104713, 10.1016/j.dsr2.2019.104713.

Almogi-Labin, A., Luz, B., Duplessy, J.C., 1986. Quaternary paleo-oceanography, pteropod preservation and stable-isotope record of the Red Sea. Palaeogeogr. Palaeoclimatol. Palaeoecol. 57 (2–4), 195–211. https://doi.org/10.1016/0031-0182(86)90013-1.

Almogi-Labin, A., Bar-Matthews, M., Shriki, D., Kolosovsky, E., Paterne, M., Schilman, B., Ayalon, A., Aizenshtat, Z., Bar-Matthews, A., 2009. Climatic variability during the last ~90 ka of the southern and northern Levantine basin as evident from marine records and speleothems. Quat. Sci. Rev. 28, 2882–2896. https://doi.org/10.1016/j.quascirev.2009.07.017.

Aloisi, G., Pierre, C., Rouchy, J.M., Foucher, J.P., Woodside, J., 2000. Methane-related authigenic carbonates of Eastern Mediterranean Sea mud volcanoes and their possible relation to gas hydrate destabilisation. Earth Planet. Sci. Lett. 184 (1), 321–338. https://doi.org/10.1016/S0012-821X(00)00322-8.

Ambrose Jr, W.G., Panieri, G., Schneider, A., Plaza-Faverola, A., Carroll, M.L., Åström, E. K., Locke, V., Carroll, J., 2015. Bivalve shell horizons in seafloor pockmarks of the last glacial-interglacial transition: a thousand years of methane emissions in the Arctic Ocean. Geochem. Geophys. Geosyst. 16 (12), 4108–4129. https://doi.org/10.1002/2015GC005980.

Archer, D.E., Maier-Reimer, E., 1994. Effect of deep-sea sedimentary calcite preservation on atmospheric CO2 concentration. Nature 367, 260–264. https://doi.org/10.1038/367260a0.

Bandel, K., Almogi-Labin, A., Hemleben, C., Deuser, W.G., 1984. The conch of *Limacina* and *Peraclis* (Pteropoda) and a model for the evolution of planktonic gastropods. Neues Jahrb. Geol. Palaeontol. Abh. 168 (1), 87–107. https://doi.org/10.1127/njgpa/168/1984/87.

Basso, D., Beccari, V., Almogi-Labin, A., Hyams-Kaphzan, O., Weissman, A., Makovsky, Y., Rueggeberg, A., Spezzaferri, S., 2020. Macro-and micro-fauna from cold seeps in the Palmahim Disturbance (Israeli off-shore), with description of *Waisiuconcha corsellii* n. sp. (Bivalvia, Vesicomyidae). Deep Sea Res. Part II 171, 104723. https://doi.org/10.1016/j.dsr2.2019.104723.

Bè, A.W.H., Gilmer, R.W., 1977. A zoographic and taxonomic review of Euthecosomatous Pteropoda. In: Ramsay, A.T.S. (Ed.), Oceanic Micropalaeontology. Academic Press, London, pp. 733–808.

Beccari, V., Basso, D., Spezzaferri, S., Rüggeberg, A., Neuman, A., Makovsky, Y., 2020. Preliminary video-spatial analysis of cold seep bivalve beds at the base of the continental slope of Israel (Palmahim Disturbance). Deep Sea Res. Part II 171, 104664. https://doi.org/10.1016/j.dsr2.2019.104664.

Beccari, V., Almogi-Labin, A., Basso, D., Panieri, G., Makovski, Y., Hajdas, I., Spezzaferri, S., 2023. Late Holocene Pteropods distribution across the base of the south eastern Mediterranean margin: the importance of the >63μm fraction. J. Micropaleontol. 42 (13–29), 2023. https://doi.org/10.5194/jm-42-13.

Bednaršek, N., Tarling, G.A., Bakker, D.C., Fielding, S., Cohen, A., Kuzirian, A., McCorkle, D., Lézé, B., Montagna, R., 2012a. Description and quantification of pteropod shell dissolution: a sensitive bioindicator of ocean acidification. Glob. Chang. Biol. 18 (7), 2378–2388. https://doi.org/10.1111/j.1365-2486.2012.02668.x.

Bednaršek, N., Tarling, G.A., Bakker, D.C.E., Fielding, S., Jones, E.M., Venables, H.J., Ward, P., Kuzirian, A., Lézé, B., Feely, R.A., Murphy, E.J., 2012b. Extensive dissolution of live pteropods in the Southern Ocean. Nat. Geosci. 5 (12), 881–885. https://doi.org/10.1038/ngeo1635.

Berger, W.H., 1978. Deep-sea carbonate: pteropod distribution and the aragonite compensation depth. Deep-Sea Res. 25 (5), 447–452.

Berger, W.H., 1979. Preservation of Foraminifera. Short Course No. 6, Society Economic. Paleontologists Mineralogists, 105–155.

Boetius, A., Ravenschlag, K., Schubert, C.J., Rickert, D., Widdel, F., Gieseke, A., Amann, R., Jorgensen, B.B., Witte, U., Pfannkuche, O., 2000. A marine microbial consortium apparently mediating anaerobic oxidation of methane. Nature 407 (6804), 623–626. https://doi.org/10.1038/35036572.

Borrelli, C., Gabitov, R.I., Liu, M.C., Hertwig, A.T., Panieri, G., 2020. The benthic foraminiferal δ34S records flux and timing of paleo methane emissions. Sci. Rep. 10 (1), 1–10. https://doi.org/10.1038/s41598-020-58353-4.

Broecker, W.S., Andree, M., Bonani, G., Wolfli, W., Klas, M., Mix, A., Oeschger, H., 1988. Comparison between radiocarbon ages obtained on coexisting planktonic

foraminifera. Paleoceanography 3 (6), 647–657. https://doi.org/10.1029/PA003i006p00647.

Burton, E.A., 1993. Controls on marine carbonate cement mineralogy: review and reassessment. Chem. Geol. 105 (1-3), 163–179.

Byrne, R.H., Acker, J.G., Betzer, P.R., Feely, R.A., Cates, M.H., 1984. Water column dissolution of aragonite in the Pacific Ocean. Nature 312, 321–326. https://doi.org/10.1038/312321a0.

Coleman, D.F., Austin Jr, J.A., Ben-Avraham, Z., Makovsky, Y., Tchernov, D., 2012. Seafloor pockmarks, deep water corals, and cold seeps along the continental margin of Israel. Oceanography 25 (1), 40–41.

Craig, H., Gordon, L.I., 1965. Deuterium and oxygen-18 variations in the ocean and the marine atmosphere. In: Tongiorgi, E. (Ed.), Stable Isotopes in Oceanographic Studies and Paleotemperatures. Spoleto, Italy, pp. 9–130.

Dessandier, P.-A., Borrelli, C., Yao, H., Sauer, S., Hong, W.-L., Panieri, G., 2020. Foraminiferal δ18O reveals gas hydrate dissociation in Arctic and North Atlantic Ocean sediments. Geo-Mar. Lett. 40 (4), 507–523.

Friedman, G.M., 1965. Occurrence and stability relationships of aragonite, high-magnesian calcite, and low-magnesian calcite under deep-sea conditions. Geol. Soc. Am. Bull. 76 (10), 1191–2119. https://doi.org/10.1130/0016-7606.

Garfunkel, Z., Arad, A., Almagor, G., 1979. The Palmahim disturbance and its regional setting. Geological Survey Israeli Bulletin, 72.

Gerhardt, S., Groth, H., Rühlemann, C., Henrich, R., 2000. Aragonite preservation in late Quaternary sediments cores on the Brazilian Continental Slope: implications for intermediate water circulation. Int. J. Earth Sci. 88 (4), 607–618.

Gerhardt, S., Henrich, R., 2001. Shell preservation of *Limacina inflata* (Pteropoda) in surface sediments from the Central and South Atlantic Ocean: a new proxy to determine the aragonite saturation state of water masses. Deep Sea Res. Part I 48 (9), 2051–2071. https://doi.org/10.1016/S0967-0637(01)00005-X.

Greinert, J., Bohrmann, G., Suess, E., 2001. Gas hydrate-associated carbonates and methane-venting at Hydrate Ridge: classification, distribution and origin of authigenic lithologies. Am. Geophys. Union 124, 99–114. https://doi.org/10.1029/GM124p0099.

Gvirtzman, Z., Reshef, M., Buch-Leviatan, O., Groves-Gidney, G., Karcz, Z., Makovsky, Y., Ben-Avraham, Z., 2015. Bathymetry of the Levant basin: interaction of salt-tectonics and surficial mass movements. Mar. Geol. 360, 25–39. https://doi.org/10.1016/j.margeo.2014.12.001.

Heaton, T.J., Köhler, P., Butzin, M., Bard, E., Reimer, R.W., Austin, W.E.N., Bronk Ramsey, C., Grootes, P.M., Hughen, K.A., Kromer, B., Reimer, P.J., Adkins, J., Burke, A., Cook, M.S., Olsen, J., Skinner, L.C., 2020. Marine20—the marine radiocarbon age calibration curve (0–55,000 cal BP). Radiocarbon 62 (4), 779–820.

Hecht, A., 1992. Abrupt changes in the characteristics of Atlantic and Levantine intermediate waters in the Southeastern Levantine Basin. Oceanol. Acta 15 (1), 25–42.

Hennekam, R., 2015. High-Frequency Climate Variability in the Late Quaternary Eastern Mediterranean: Associations of Nile Discharge and Basin Overturning Circulation Dynamics (Doctoral dissertation). Utrectct Studies in Earth Science, Department of Earth Sciences, p. 78.

Hovland, M., Svensen, H., Forsberg, C.F., Johansen, H., Fichler, C., Fosså, J.H., Jonsson, R., Rueslåtten, H., 2005. Complex pockmarks with carbonate-ridges off mid-Norway: Products of sediments degassing. Mar. Geol. 218 (1–4), 191–206. https://doi.org/10.1016/j.margeo.2005.04.005.

Kastner, M., Elderfield, H., Martin, J. B., Suess, E., Kvenvolden, K.A., Garrison, R.E., 1990. Diagenesis and interstitial-water chemistry at the Peruvian continental margin—major constituents and strontium isotopes. In: Suess, E., von Huene, R., et al. (eds.), Proceedings Ocean Drilling Program, Scientific Results. 112, 413-440.

Krumgalz, B.S., Erez, J., 1984. Chemical oceanography survey of the northern Red Sea, the Straits of Tiran and the Gulf of Elat. Israelian Oceanogr. Limnol. Res., Haifa, Report 3 (84), 1–133.

Lawal, M.A., Bialik, O.M., Lazar, M., Waldmann, N.D., Foubert, A., Makovsky, Y., 2023. Modes of gas migration and seepage on the salt-rooted Palmahim Disturbance, southeastern Mediterranean. Mar. Pet. Geol. 153, 106256.

Luff, R., Wallmann, K., Aloisi, G., 2004. Numerical modeling of carbonate crust formation at cold vent sites: significance for fluid and methane budgets and chemosynthetic biological communities. Earth Planet Sci. Lett. 221 (1-4), 337–353.

Makovsky, Y., Rüggeberg, A., Bialik, O., Foubert, A., Almogi-Labin, A., Alter, Y., Bampas, V., Basso, D., Feenstra, E., Fentimen, R., Friedheim, O., Hall, E., Hazan, O., Herut, B., Kallergis, E., Karageorgis, A., Kolountzakis, A., Manousakis, L., Nikolaidis, M., Pantazoglou, F., Rahav, E., Renieris, P., Schleinkofer, N., Sisma Ventura, G., Stasnios, V., Weissman, A. and the EUROFLEETS2 SEMSEEP participants, (2016). South East Mediterranean SEEP Carbonate. R/V AEGAEO, Cruise EUROFLEETS2 SEMSEEP, 20.09. – 01.10.2016, Piraeus (Greece) – Piraeus (Greece) Cruise Summary Report, 1-62.

Manno, C., Sandrini, S., Tositti, L., Accornero, A., 2007. First stages of degradation of *Limacina helicina* shells observed above the aragonite chemical lysocline in Terra Nova Bay (Antarctica). J. Mar. Syst. 68 (1–2), 91–102. https://doi.org/10.1016/j.jmarsys.2006.11.002.

Martin, W.R., Sayles, F.L., 1996. CaCO3 dissolution in sediments of the Ceara Rise, western equatorial Atlantic. Geochim. Cosmochim. Acta 60, 243–263. https://doi.org/10.1016/0016-7037(95)00383-5.

McCrea, J.M., 1950. On the isotopic chemistry of carbonates and a paleotemperature scale. J. Chem. Phys. 18 (6), 849–857.

Milliman, J.D., Ross, D.A., Ku, T.L., 1969. Precipitation and lithification of deep-sea carbonates in the Red Sea. J. Sediment. Res. 39 (2), 724–736. https://doi.org/10.1306/74D71CFD-2B21-11D7-8648000102C1865D.

Missiaen, L., Wacker, L., Lougheed, B.C., Skinner, L.C., Hajdas, I., Nouet, J., Pichat, S., Waeebroeck, C., 2020. Radiocarbon dating of small-sized foraminifer samples:

insights into marine sediment mixing. Radiocarbon 62 (2), 313–333. https://doi.org/10.1017/RDC.2020.13.

Mojtahid, M., Manceau, R., Schiebel, R., Hennekam, R., De Lange, G.J., 2015. Thirteen thousand years of southeastern Mediterranean climate variability inferred from an integrative planktic foraminiferal-based approach. Paleoceanography 30 (4), 402–422. https://doi.org/10.1002/2014PA002705.

Naehr, T.H., Eichhubl, P., Orphan, V.J., Hovland, M., Paull, C.K., Ussler III, W., Lorenson, T., Greene, H.G., 2007. Authigenic carbonate formation at hydrocarbon seeps in continental margin sediments: a comparative study. Deep Sea Res. Part II 54 (11–13), 1268–1291. https://doi.org/10.1016/j.dsr2.2007.04.010.

Oakes, R.L., Peck, V.L., Manno, C., Bralower, T.J., 2019. Degradation of internal organic matter is the main control on pteropod shell dissolution after death. Global Biogeochem. Cycles 33 (6), 749–760. https://doi.org/10.1029/2019GB006223.

Ohkushi, K., Uchida, M., Shibata, Y., 2017. Radiocarbon age differences between benthic-planktonic foraminifera in sediment cores from the Shatsky Rise, central North Pacific. J. Sedimentol. Soc. Japan 76 (1), 17–27.

Ozer, T., Gertman, I., Kress, N., Silverman, J., Herut, B., 2017. Interannual thermohaline (1979–2014) and nutrient (2002–2014) dynamics in the Levantine surface and intermediate water masses, SE Mediterranean Sea. Global Planet. Change 151, 60–67. https://doi.org/10.1016/j.gloplacha.2016.04.001.

Ozer, T., Gertman, I., Gildor, H., Goldman, R., Herut, B., 2020. Evidence for recent thermohaline variability and processes in the deep water of the Southeastern Levantine Basin, Mediterranean Sea. Deep Sea Res. Part II 171, 104651. https://doi.org/10.1016/j.dsr2.2019.104651.

Panieri, G., Graves, C.A., James, R.H., 2016a. Paleo-methane emissions recorded in foraminifera near the landward limit of the gas hydrate stability zone offshore western Svalbard. Geochem. Geophys. Geosyst. 17 (2), 521–537. https://doi.org/10.1002/2015GC006153.

Panieri, G., Lepland, A., Whitehouse, M.J., Wirth, R., Raanes, M.P., James, R.H., Graves, C.A., Crémière, A., Schneider, A., 2016b. Diagenetic Mg-calcite overgrowths on foraminiferal tests in the vicinity of methane seeps. Earth Planet. Sci. Lett. 458, 203–212. https://doi.org/10.1016/j.epsl.2016.10.024.

Panieri, G., Bünz, S., Fornari, D.J., Escartin, J., Serov, P., Jansson, P., Torres, M.E., Johnson, J.E., Hong, W., Sauer, S., Garcia, R., Gracias, N., 2017. An integrated view of the methane system in the pockmarks at Vestnesa Ridge, 79 N. Mar. Geol. 390, 282–300. https://doi.org/10.1016/j.margeo.2017.06.006.

Peckmann, J., Reimer, A., Luth, U., Luth, C., Hansen, B.T., Heinicke, C., Hoefs, J., Reitner, J., 2001. Methane-derived carbonates and authigenic pyrite from the northwestern Black Sea. Mar. Geol. 177 (1-2), 129–150.

Richter, G., 1976. Zur Frage der verwandtschaftsbeziehungen von Limacinidae und Cavoliniidae (Pteropoda: thecosomata). Archiv Für Molluskenkunde 107 (1–3), 137–144.

Roether, W., Klein, B., Manca, B.B., Theocharis, A., Kioroglou, S., 2007. Transient Eastern Mediterranean deep waters in response to the massive dense-water output of the Aegean Sea in the 1990s. Progr. Oceanogr. 74, 540–571. https://doi.org/10.1016/j.pocean.2007.03.001.

Rubin-Blum, M., Antler, G., Turchyn, A.V., Tsadok, R., Goodman-Tchernov, B.N., Shemesh, E., Austin, J.A., Coleman, D.F., Makovsky, Y., Sivan, O., Tchernov, D., 2014. Hydrocarbon-related microbial processes in the deep sediments of the Eastern Mediterranean Levantine Basin. FEMS Microbiol. Ecol. 87 (3), 780–796. https://doi.org/10.1111/1574-6941.12264.

Rutten, A., 2001. Fluxes, diagenesis and preservation of recent and Holocene sediments in the Eastern Mediterranean. Geologica Ultraiectina, (Doctoral dissertation), 202, 1–176.

Schattner, U., Lazar, M., 2016. Hierarchy of source-to-sink systems - Examples from the Nile distribution across the eastern Mediterranean. Sedimentary Geology 343, 119–131. https://doi.org/10.1016/j.sedgeo.2016.08.006.

Schneider, A., Crémière, A., Panieri, G., Lepland, A., Knies, J., 2017. Diagenetic alteration of benthic foraminifera from a methane seep site on Vestnesa Ridge (NW Svalbard). Deep Sea Res. Part I 123, 22–34. https://doi.org/10.1016/j.dsr.2017.03.001.

Schneider, A., Panieri, G., Lepland, A., Consolaro, C., Crémière, A., Forwick, M., Johnson, J.E., Plaza-Faverola, A., Sauer, S., Knies, J., 2018. Methane seepage at Vestnesa Ridge (NW svalbard) since the last glacial maximum. Quat. Sci. Rev. 193, 98–117. https://doi.org/10.1016/j.quascirev.2018.06.006.

Sisma-Ventura, G., Bialik, O.M., Makovsky, Y., Rahav, E., Ozer, T., Kanari, M., Marmen, S., Blekin, N., Guy-Haim, T., Antler, G., Herut, B., 2022. Cold seeps alter the near-bottom biogeochemistry in the ultraoligotrophic Southeastern Mediterranean Sea. Deep Sea Res. Part I: Oceanogr. Res. Papers 103744. https://doi.org/10.1016/j.dsr.2022.103744.

Skliris, N., 2014. Past, present and future patterns of the thermohaline circulation and characteristic water masses of the Mediterranean Sea. In: Goffredo, S., Dubinsky, Z. (Eds.), The Mediterranean Sea: Its History and Present Challenges. DE.Springer, Berlin, pp. 29–48. https://doi.org/10.1007/978-94-007-6704-1_3.

Spiro, B., Ezra, O., Najorka, J., Delgado, A., Bialik, O., Ben-Avraham, Z., Coleman, D., Makovsky, Y., 2021. Mineralogical, chemical and stable C and O isotope characteristics of surficial carbonate structures from the Mediterranean offshore Israel indicate microbial and thermogenic methane origin. Geo-Mar. Lett. 41 (1), 1–17. https://doi.org/10.1007/s00367-021-00684-w.

Torres, M.E., Mix, A.C., Kinports, K., Haley, B., Klinkhammer, G.P., McManus, J., de Angelis, M.A., 2003. Is methane venting at the seafloor recorded by δ13C of benthic foraminifera shells? Paleoceanography 18 (3), 1062. https://doi.org/10.1029/2002PA000824.

Van der Spoel, S., 1972. Notes on the identification and speciation of Heteropoda (Gastropoda). Zoologische Mededelingen 47 (45), 545–560.

Van der Spoel, S., 1976. Finer sculptures in euthecosomatous shells, and their value for taxonomy (Mollusca, Pteropoda). Beaufortia 24 (314), 105–121.

Wessel, P., Smith, W.H.F., Scharroo, R., Luis, J., Wobbe, F., 2013. Generic mapping tools: improved version released. Eos Trans. AGU 94 (45), 409–410.

Wormuth, J.H., 1981. Vertical distributions and diel migrations of Euthecosomata in the northwest Sargasso Sea. Deep Sea Res. Part A 28 (12), 1493–1515. https://doi.org/10.1016/0198-0149(81)90094-7.

Zavatarelli, M., Mellor, G.L., 1995. A numerical study of the Mediterranean Sea circulation. J. Phys. Oceanogr. 25, 1384–1414. https://doi.org/10.1175/15200485(1995)025<1384:ANSOTM>2.0.CO;2.